





# Long-Range Daytime 3D Imaging Lidar With Short Acquisition Time Based on $64 \times 64$ Gm-APD Array

Changsheng Tan , Wei Kong , Genghua Huang, Jia Hou, Yongfeng Luo, Tao Chen , Xialin Liu, and Rong Shu 

**Abstract**—This paper reports a complete solution for short-acquisition-time, flood-illumination, and non-scanning 3D imaging. Based on an InGaAs/InP  $64 \times 64$  Geiger-mode avalanche photodiode array, we developed a single-photon imaging Lidar with a field of view of 19.2 mrad. A spatiotemporal dominant imaging method was also applied for depth estimation under high daytime background noise conditions. In the field tests, 3D imaging information was effectively extracted from objects with strong solar background light. An acquisition time of only 0.5 ms to 4 ms was needed for a building target approximately 1300 m away. The experimental results show that the Lidar and its data processing method have the potential for dynamic scenarios that require high performance 3D imaging, such as vehicle navigation, airborne mapping, and moving target monitoring.

**Index Terms**—3D imaging, depth estimation, Gm-APD array, LiDAR, single-photon detection.

## I. INTRODUCTION

**L**IGHT detection and ranging (Lidar) has become an important tool for high resolution range measurement and 3D imaging owing to its excellent angular and range resolution, it is widely applied in fields such as robotic identification, intelligent transportation, and spacecraft navigation [1]–[3]. Most commercial Lidars use avalanche photodiodes (APD) with a gain from tens to hundreds to acquire the scattered signal. These Lidars with relatively low gain generally have higher single

pulse energy to achieve long range measurement [4]. Their small number of beams and low laser repetition rate makes it difficult for such detectors to make high resolution 3D imaging measurements at long distances.

By using single photon sensitive detectors, Lidar can be designed to have more beams, a higher repetition rate, and larger detection range [5]. For example, Li *et al.* developed a single photon scanning Lidar working at 1550 nm and received the echo using a single pixel InGaAs single-photon avalanche diode, achieving 3D imaging over 200 km [6]. Sigma Space Corporation developed several single photon sensitive Lidars that simultaneously emitted 100 beams for range measurement [7]. These Lidars have the ability to map the ground surface from aircraft at heights of several kilometers with effective pulse rates up to 6 MHz, which greatly improves the performance of commercial Lidars. In addition, with the development of large-scale avalanche focal plane array integration technology in recent years, the non-scanning planar-array-based photon-counting Lidar is also considered as a feasible method for realizing efficient active 3D imaging, with a fast imaging speed and wide field of view [8], [9]. The planar-array-based Lidar can image the whole scene in one laser illumination shooting, which permits high reliability 3D imaging without any blurring when the detection target or equipment platform is dynamic. Henriksson *et al.* demonstrated high-resolution 3D imaging of a 340 m natural target under daylight conditions by using a  $32 \times 32$  Geiger-mode array camera [10]. Recently, Tobin *et al.* developed a 3D depth imaging device that is based on a  $32 \times 32$  InGaAs/InP SPAD array. Benefiting from the developed M2R3D algorithmic framework, it can make the 3D imaging over 150 meters under the occlusion of strong attenuating media [11]. The design of a small number of transceivers combined with scanning provides a better signal-to-background ratio, because energy of the laser is concentrated in a few beams, while non-scanning flash imaging designs realize higher data frame rates, which makes it possible to quickly form 3D images.

However, solar background irradiation has a great influence on single-photon Lidars with extremely high detection sensitivity. In its data processing, it is especially important to algorithmically separate the signal and noise photons [12], [13]. In addition, it is very challenging to retrieve depth images from sparse photon events through advanced imaging algorithms when the number of signal photons is as low as approximately 1 or less per pixel in the 3D imaging area [14]. Some efficient single-photon depth and reflectivity estimation algorithms have been proposed in recent years that deserve attention. Examples

Manuscript received March 17, 2022; revised April 7, 2022; accepted April 8, 2022. Date of publication April 12, 2022; date of current version April 26, 2022. This work was supported in part by the Science and Technology Commission of Shanghai Municipality under Grant 2019SHZDZX01, in part by the National Natural Science Foundation of China under Grants 61805268 and 61875219, in part by the Innovation Foundation of Shanghai Institute of Technical Physics, Chinese Academy of Sciences under Grant CX-368, and in part by Shanghai Scientific Research Foundation under Grant 19ZR1466000. (Corresponding author: Wei Kong.)

Changsheng Tan is with the Key Laboratory of Space Active Opto-Electronics Technology and Shanghai Institute of Technical Physics, Chinese Academy of Sciences, Shanghai 200083, China, and also with the University of Chinese Academy of Sciences, Beijing 100049, China (e-mail: tanchangsheng@mail.sitp.ac.cn).

Wei Kong, Genghua Huang, Tao Chen, and Rong Shu are with the Key Laboratory of Space Active Opto-Electronics Technology and Shanghai Institute of Technical Physics, Chinese Academy of Sciences, Shanghai 200083, China, with the University of Chinese Academy of Sciences, Beijing 100049, China, and also with the Shanghai Research Center for Quantum Sciences, Chinese Academy of Sciences, Shanghai 201315, China (e-mail: kongwei@mail.sitp.ac.cn; genghuah@mail.sitp.ac.cn; chentao@sitp.ac.cn; shurong@mail.sitp.ac.cn).

Jia Hou, Yongfeng Luo, and Xialin Liu are with the Key Laboratory of Space Active Opto-Electronics Technology and Shanghai Institute of Technical Physics, Chinese Academy of Sciences, Shanghai 200083, China (e-mail: houjia@mail.sitp.ac.cn; luoyongfeng@mail.sitp.ac.cn; 1194226717@qq.com).

Digital Object Identifier 10.1109/JPHOT.2022.3166807

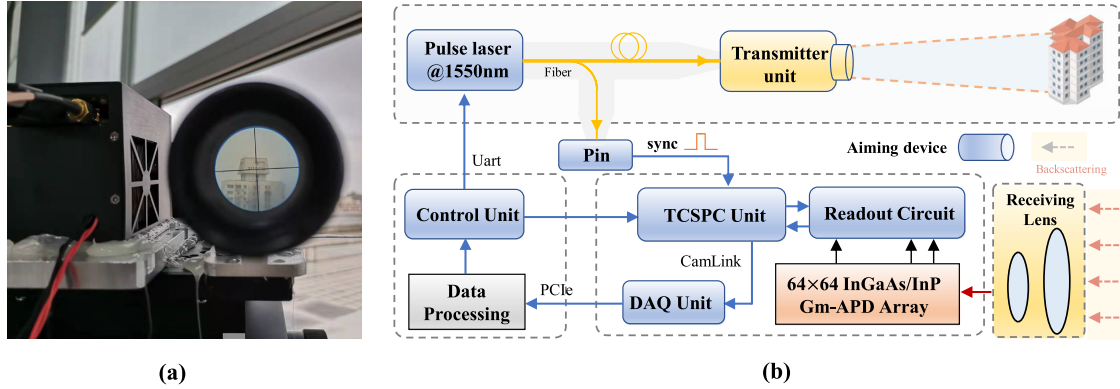


Fig. 1. Proposed 3D imaging Lidar: (a) Through the auxiliary calibration of a large-aperture collimator, the sighting telescope is coaxially placed next to the Lidar. (b) Schematic diagram of the system.

include the first-photon imaging proposed by Kirmani *et al.* and the photon-efficient computational imaging work of Shin *et al.*, which demonstrated the potential for depth recovery in the photon-limited case [15], [16]. Among these, Kirmani *et al.* developed a computational imaging method that has the ability to recover the depth and gray image while only one photon event is required per pixel. This algorithm exploits the spatial correlation of real-world objects to achieve photon limited imaging with high background noise, which has great value in long-distance and super-resolution 3D imaging [17].

Both the photon arrival observation model of individual pixels and the spatial correlation between adjacent pixels can be applied to photon 3D imaging. From the perspective of planar-array-based photon-counting Lidars, imaging efficiency is improved and the acquisition time reduced. In this study, a single-photon 3D imaging Lidar was developed based on a  $64 \times 64$  Gm-APD array. By exploiting the spatiotemporal correlation of the arrival of photons at neighboring pixels in the Gm-APD array, a practical 3D reconstruction strategy for planar-array-based imaging Lidar is presented. The framework can effectively extract the signal photons from strong solar background noise and recover the depth image while the data acquisition time is limited. The system structure, algorithm framework, and field experimental results will be described in detail below.

## II. INSTRUMENTAL DESCRIPTION

Fig. 1 shows the non-scanning 3D imaging Lidar based on a  $64 \times 64$  InGaAs/InP Gm-APD array developed by the Shanghai Institute of Technical Physics, Chinese Academy of Sciences. Its major parameters are listed in Table I. The Lidar's transmitter emits a pulsed laser beam with a wavelength of 1550 nm and a repetition rate of 20 kHz from a homemade fiber laser. Its divergence angle is adjusted by the transmitting lens to cover the receiving field of view. Echo signals scattered from the target are filtered using a filter with 2 nm bandwidth focused on the photosensitive surface of the detector module by a receiving lens. The detector module has a resolution of  $64 \times 64$ . The receiver's field of view is 19.2 mrad with a single pixel field of view of 0.3 mrad.

The Lidar's detector module is an integrated device that includes an InGaAs Gm-APD array chip, an integrated quenching

TABLE I  
MAJOR SPECIFICATIONS OF THE LIDAR SYSTEM

Transmitter	
Laser wavelength	1550 nm
Repetition rate	20 kHz
Pulse energy	$60 \mu\text{J}$
Pulse duration	2 ns
Laser divergence	20 mrad
Receiver	
Receiver aperture	34 mm
Focal length of receiving lens	166 mm
Resolution of detector array	$64^*64$
Adjacent pixel distance	$50 \mu\text{m}$
Total field of view	19.2 mrad
Single pixel field of view	0.3 mrad
Bandwidth of the filter	2 nm

circuit, and a time-to-digital converter (TDC) chip. Photons incident on each pixel of the Gm-APD array chip are converted into electrical pulses. The probability (per pixel) is approximately 20% and is defined as the photon detection efficiency (PDE). The TDC chip measures the time difference between the start signal and the photon events at every pixel after a programmable time delay, to realize the time-correlated single photon counting (TCSPC) measurement. The start signal is generated from the detector that is installed in the transmitting optical path. The TDC chip has a time resolution of 1 ns and quantization bits of 12 bits, corresponding to a time measurement range of  $4 \mu\text{s}$  or a distance range of 600 m. Because the TDC chip can only acquire one photon event per pixel at every acquisition cycle, photons scattered by the target may be hidden by solar background photons that arrive first. Finally, the photon events from target scattering and the solar background are transferred to the computer via a CameraLink cable.

For this system, with a detection distance of  $R$ , the average number of photons scattered from the target that are detected by a single pixel are:

$$N_s = \eta_t \eta_r \eta_{\text{det}} \times \frac{P_{tr}}{hc/\lambda} \times \frac{\pi D^2}{4R^2} \times \frac{\rho}{\pi} \times \frac{0.2\theta_r^2}{\pi\theta_t^2/4} \times \exp\left[-2 \int_0^R \alpha(z) dz\right] \quad (1)$$

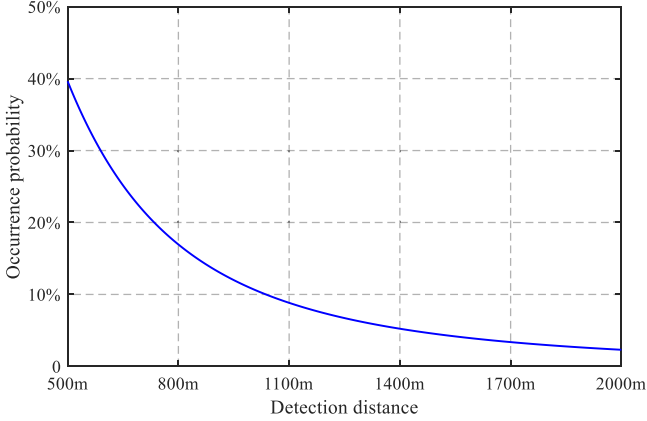


Fig. 2. Occurrence probability of signal photons from range of 500 to 2000 m.

where  $\eta_t$  and  $\eta_r$  are the optical efficiencies of the transmitting and receiving units, and  $\eta_{det}$  is the PDE of the detector. The second term is the total number of emitted photons, where  $P_{tr}$  is the transmitting energy of the single pulse,  $h$  is the Planck constant,  $c$  is the speed of light, and  $\lambda$  is the laser wavelength.  $D$  is the effective receiving aperture of the receiving lens,  $\rho$  is the backscattering reflectivity of the target surface,  $\theta_r$  is the single pixel field of view,  $\theta_t$  is the emitted laser divergence angle, and the constant 0.2 is the effective area fill factor of the detector that considers the micro-lens structure and F number of the receiving optical system. The last term is the dual-way atmospheric transmittance between the Lidar and the target, where  $\alpha$  is the extinction coefficient of the atmosphere.

Fig. 2 shows the theoretically estimated variations of the single pixel occurrence probability of signal photons from 500 to 2000 m without considering the ambient background photons. It equals  $1 - e^{-N_r}$  according to the Poisson distribution characteristics of photons. In the calculation, the backscattering reflectivity  $\rho$  is assumed to be 0.2 at 1550 nm, and the extinction coefficient at 1550 nm is assumed to be 0.1 km<sup>-1</sup> corresponding to typical urban conditions [18]. The estimated probability drops to < 10% at distances > 1 Km.

During daytime observations, the occurrence probability of signal photons may be further reduced by solar background while the non-signal photon events occur earlier than signal photons, for the constraint that the TDC chip acquires at most one event within one acquisition cycle. In strong ambient background light conditions the number of solar background photons at a time interval  $\Delta T$  can be written as

$$N_e = \eta_r \eta_{det} \times \frac{S_B \delta \lambda \Delta T}{hc/\lambda} \times \frac{\pi D^2}{4} \times 0.2 \theta_r^2 + P_{dark} \Delta T \quad (2)$$

where  $S_B$  is the scattered solar irradiance at 1550 nm, which can be estimated from the product of the earth surface solar irradiance at 1550 nm and the target directional reflectance.  $\delta \lambda$  is the bandwidth of the filter. The second term comes from the detector's dark counts, where  $P_{dark} \approx 20$  kHz, which is the single pixel dark count rate of the detector. During daytime, noise photon events mainly come from solar background. Here we set the spectral irradiance of the sun at ground level as 0.25

$W/m^2/nm$  at 1550 nm, and the directional reflectance as  $0.2/\pi$ . Their product of  $S_B = 16$  mW/m<sup>2</sup>/nm/sr. Assuming that the target is located near the center of the strobe gate, which means that  $\Delta T \approx 2 \mu s$ , then the average noise photons between the start time of the gate and the signal photon occurrence time is 0.8, which means that there is a 56% probability that the noise photon event occurs before the signal photon event. This also shows that the occurrence probability of signal photons will be further reduced by approximately 50% for the daytime solar background. At distance larger than 1 km, the signal photon occurrence ratio may drop to only several percent at high ambient conditions. The theoretical model demonstrates the expected performance of the lidar system, as well as the impact from strong solar background noises. It shows that the lidar system has a relatively low signal detection probability and relatively high noise signal occurrence at strong solar background conditions, which poses a challenge to data processing.

### III. IMAGING STRATEGIES

Since the echo energy of the Lidar is distributed over 64×64 pixels, the single pixel photon occurrence probability at long range is considerably reduced. The imaging algorithm needs to extract signal photons from a large number of noise photons and estimate the distance with as few frames of data as possible. Several distance extraction methods for photon-counting Lidars have been proposed in the literature. The maximum peak detection approach performs a depth estimation by finding the peak position from a histogram accumulated by a large number of recorded photon events [19]. For the tiny number of photon events in a short acquisition time, multiple peaks occur for the low signal to noise ratio of the data. The probability of the true distance being wrongly estimated or missed is considerably increased. The matched filtering method retrieves depth information by comparing the Lidar echo with the Lidar impulse response function and identifies the target position with the strongest correlation [20]. This method needs to measure the impulse response function that is determined by the laser pulse shape and detector jitter. It has better performance than the peak detection method and can increase the probability of correct identification. Besides, some novel statistical-model-based estimation frameworks combined with spatial correlation characteristics have been proposed. For example, by introducing the strategy of non-uniform sampling and the non-local spatial correlation between patches, Chen *et al.* improves the quality of depth reconstruction in the case of photon-starved or missing scanned spatial points [21].

Recently, Shin *et al.* developed a photon-limited estimation method supported by global optimization theory [16]. It extracts the range estimation of sparse profile contours as a convex optimization problem, which further reduces the requirement for the number of signal photons in large detection scenarios. This approach is used in several beam-scanning single photon Lidar systems [22], [23]. In this study, we apply this method in a planar-array-based photon-counting Lidar for the 3D information extraction. The algorithm has a multi-level correlation filtering mechanism for signal photon extraction at high



ambient background conditions. Moreover, benefitting from the spatial correlation of adjacent pixels and temporal correlation of adjacent laser pulses, only a few photons are required for 3D reconstruction. This algorithm is divided into three steps, initial range correction, photon set extraction, and optimal depth estimation.

### A. Initial Range Correction

A coarse depth is set as the peak position of the histogram statistics. For the low signal to noise ratio of a single pixel, the photon events at surrounding pixels are also included for statistics. We select a  $3 \times 3$  area centered at the pixel  $(i, j)$  to count the number of photons in different range bins, where  $i$  and  $j$  are the pixel subscripts of the detector. At a few frames, the statistical curve  $S_{ij}(z)$  is generally discontinuous so that the peak position is hard to distinguish. We use the instrumental response function  $w(z)$  to complete the cross-correlation operation and get a smooth statistical result  $S'_{ij}(z)$ . The instrumental response function is obtained by accumulating hard target signals at multiple frames in the laboratory. Assuming that  $z_s$  is the depth corresponding to the peak of the sequence  $S'_{ij}(z)$ ,  $c$  is the speed of light, the total width of the echo impulse response generated in this region is  $w_d$ , and the sequence range of the retained photons in pixel  $(i, j)$  can be expressed as:

$$\mathbf{Q}_{i,j}^n = \{e_k; |e_k - 2z_s/c| \leq w_d/2\}, s = \arg \max_{z_s} S'_{ij}(z) \quad (3)$$

In the photon-limited cases, the ensemble  $\mathbf{Q}_{i,j}^n$  ensures that more signal photons are included as possible, although many noise photons may also be included.

### B. Photon Set Extraction

In this step, a photon dataset is constructed for the optimal estimate that excludes noise photons. The dataset is designed loosely to retain more suspected signal photon events. For the pixel  $(i, j)$ , we select the photon events of pixel  $(i, j)$  that are located within the effective width of the instrumental response function around the peak position. In addition to the photons corresponding to the range limited by the pixel  $(i, j)$ , photons falling within the distance interval defined by the adjacent eight pixels are also extracted as the signal photon dataset  $R_{i,j}$ . Although the photon dataset may include some noise photons, the coarse depth's constraints on the optimal estimation algorithm can be reduced.

For each pixel, the photons in the new dataset are then counted to renew the statistical curve  $P_{ij}(z)$ . Then the cross-correlation operation with the instrumental response function  $w(z)$  is rebuilt to renew a smooth statistical result  $P'_{ij}(z)$ . Here we keep the photons  $e_t^{i,j}$  located near the peak of  $P'_{ij}$  similar to Step.1. Note that these photons originate only from the pixel  $(i, j)$  own photon set, avoiding over-saturation of the central pixel data set to be estimated by neighboring photons, which is crucial to maintain the spatial resolution. Then, the obtained photon set  $U_{i,j}$  with a high signal-to-noise ratio can be expressed as:

$$U_{i,j} = \left\{ e_t^{i,j} : \left| e_t^{i,j} - e_t^{R(i,j)} \right| < \alpha * IRF_w \right\} \quad (4)$$

where  $e_t^{R(i,j)}$  is defined as the median photon time-of-flight of neighboring pixels within the regional grid.  $\alpha$  is the broadening factor, which determines the tolerance of the estimated photon set. The preliminary response photons from the above search are reviewed, which can be set as the initial value to carry out the optimal estimation in step 3.

### C. Optimal Depth Estimation

For extremely weak echoes in the receiver, the process of a single photon arriving at the detector is similar to the Poisson distribution. Assume that the arrival pulse observation model is  $s(t)$ , and  $T_r$  is the width of the effective receiving time per pulse. Here, the average signal photon per pulse is  $N_s = \int_0^{T_r} s(t) dt$ , and the response photon per pulse from the noise is  $N_e = (\eta n_b + n_d) T_r$ , where  $n_b$  indicates the count of background noise photons,  $n_d$  denotes the dark count of the system, and  $\eta$  is the quantum efficiency. Assume that the echo pulse is within the  $T_r$ , and that  $z_{i,j}$  denotes the actual depth. Therefore, the probability of not detecting a photon per pulse for pixel  $(i, j)$  is  $e^{-(\eta x_{i,j} N_s + N_e)}$ , where  $x_{i,j}$  represents the reflectivity of the irradiation point. For pixel  $(i, j)$  in the detector, its corresponding received luminous flux can be expressed as

$$r_{i,j}(t) = x_{i,j} s(t - 2z_{i,j}/c) + n_b \quad (5)$$

The detection rate of photons under the Poisson distribution can be expressed as  $d_{i,j}^r(t)$ , and the recorded photon located within the strobe gate can be expressed as

$$m(0, T_r) = \int_0^{T_r} d_{i,j}^r(t) dt = \int_0^{T_r} [(\eta r_{i,j}(t) + n_d(t))] dt \quad (6)$$

The previous filtering operation effectively improves the signal-to-noise ratio of the estimated photon set, while substantially reducing the intensity of the recorded photons, at which point  $m(0, T_r)$  is weak. Therefore, the observation model of the detection system can be expressed as  $y \sim \text{Poisson}(m(0, T_r))$ . The negative logarithmic maximum likelihood (ML) function of the photon time-of-flight has the following form:

$$L(z_{i,j} | t_{i,j}^U) = - \sum_{i,j}^{U_{i,j}} \log [s(t_{i,j}^U - 2z_{i,j}/c)], t_{i,j}^U = e_{i,j}^U + T_{de} \quad (7)$$

where  $z_{i,j}$  is the distance information to be estimated, and  $T_{de}$  is the time delay of the system. The above regularized ML estimation model can be converted to the following convex optimization solution problem:

$$\hat{z} = \arg \min_{z_{i,j}} \sum_{i=1}^m \sum_{j=1}^n L(z_{i,j} | \{t_{i,j}\}_{\mathbf{H}} \in U_{i,j}) + \beta \text{pen}(z_{i,j}) \quad (8)$$

subject to  $z_{i,j} \in (0, T_r)$ , where  $\text{pen}(z_{i,j})$  is the convex function used to penalize the smoothness of the depth profile. The total variation regularization term  $\|z_{i,j}\|_{TV}$  is used for this constraint solution.  $\beta$  is a weighting factor that regulates the degree of influence of the penalty term. Here, we solved this convex optimization problem by adopting the SPIRAL-TAP solver, which is an efficient Poisson distribution-based reconstruction

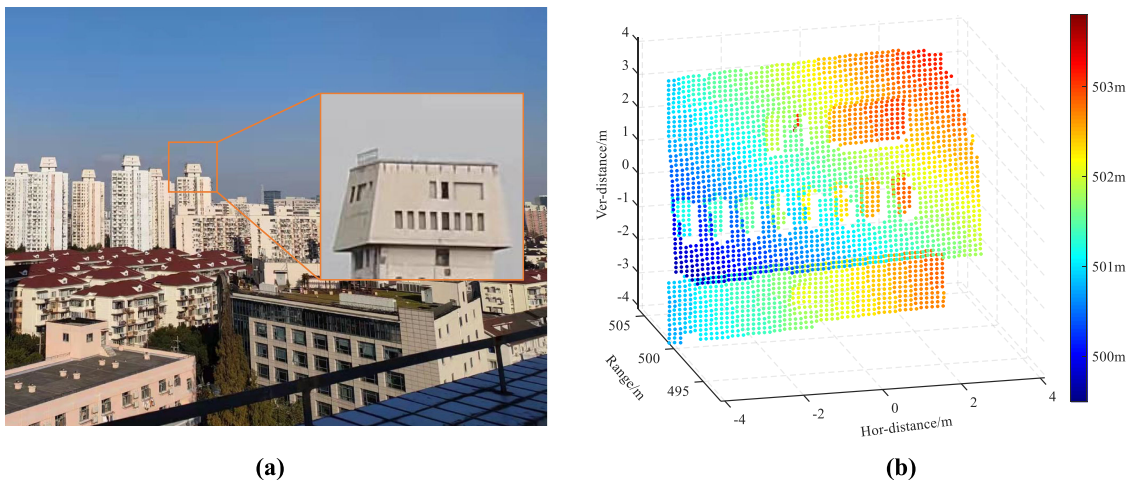


Fig. 3. Imaging target in the experiment: a roof marker of approximately 500 m distance. At this time, the timing-delay was  $3 \mu\text{s}$ , and the strobe gate was 1000 ns. (a) Experimental scene, and (b) Reference 3D point cloud distribution obtained by the system.

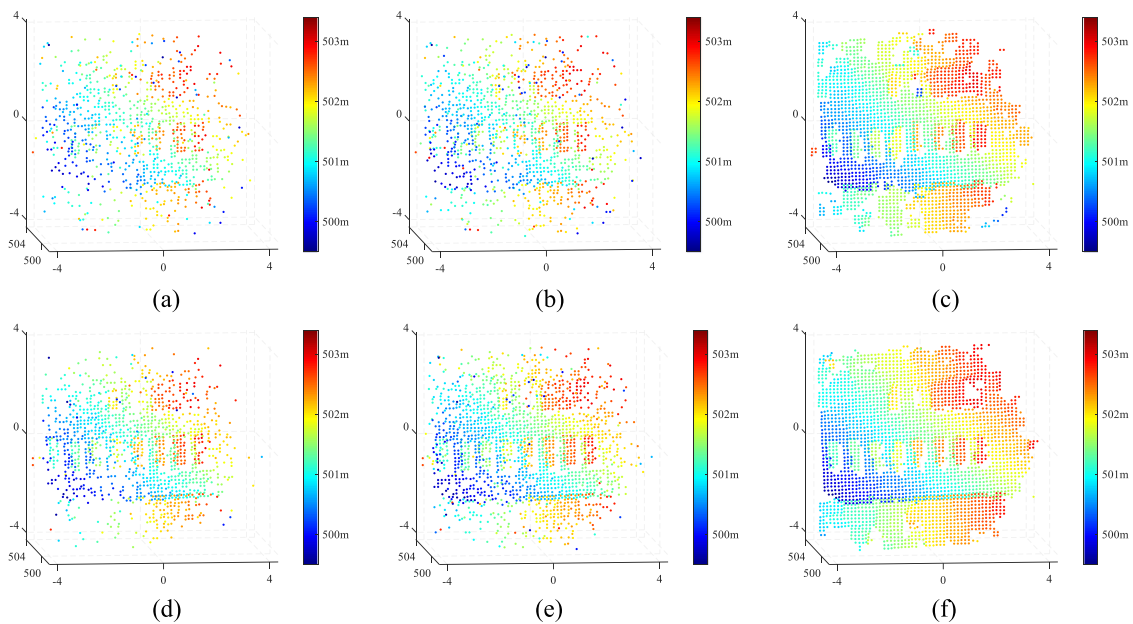


Fig. 4. Results of different extraction strategies using 20 frame and 50 frame pulses: (a)-(c), respectively, correspond to peak picking, matched filtering and the improved spatiotemporal dominant reconstruction strategy after 20 frame pulses, i.e., 1 ms acquisition time. Similarly, (d)-(f) correspond to the results of 50 frame pulses.

algorithm that has shown great recovery performance in several studies [24]. Due to the limited number of recording photons, the framework only retains the pixels with effective initial depth in set  $U_{i,j}$  to avoid the reduction of spatial resolution. The solution result  $z_{i,j}$  will be regarded as the global optimal estimation of pixels  $(i, j)$ .

#### IV. EXPERIMENTAL DEMONSTRATION

After calibration in the laboratory, the Lidar system was pointed to the target buildings to evaluate the performance during daytime. Fig. 3(a) shows the visible image of the Lidar pointing area. The laser spot irradiated the roof of a building approximately 500 m north of the system. We used results from

1000 frames of data at an accumulation time of 50 ms as the reference 3D image of the target. The extracted signal photons per pixel were approximately 188 at 1000 frames with average occurrence probability of 18.8% per pulse per pixel. For the large photons under relatively long observation times, the extracted image shown in Fig. 3(b) clearly reveals the 3D shape of the target.

At frames of only 20 and 50, corresponding to an accumulation time of 1 ms and 2.5 ms, respectively, the extracted photons decreased to 3.8 and 9.4 per pixel, respectively. Comparing with the reference depth profile, the extracted signal photons were distributed sparsely while only 0.8 and 2.1 signal photons on average were located within  $\pm 3$  ns of the reference position. Fig. 4 shows the 3D depth results by the above imaging algorithm for a

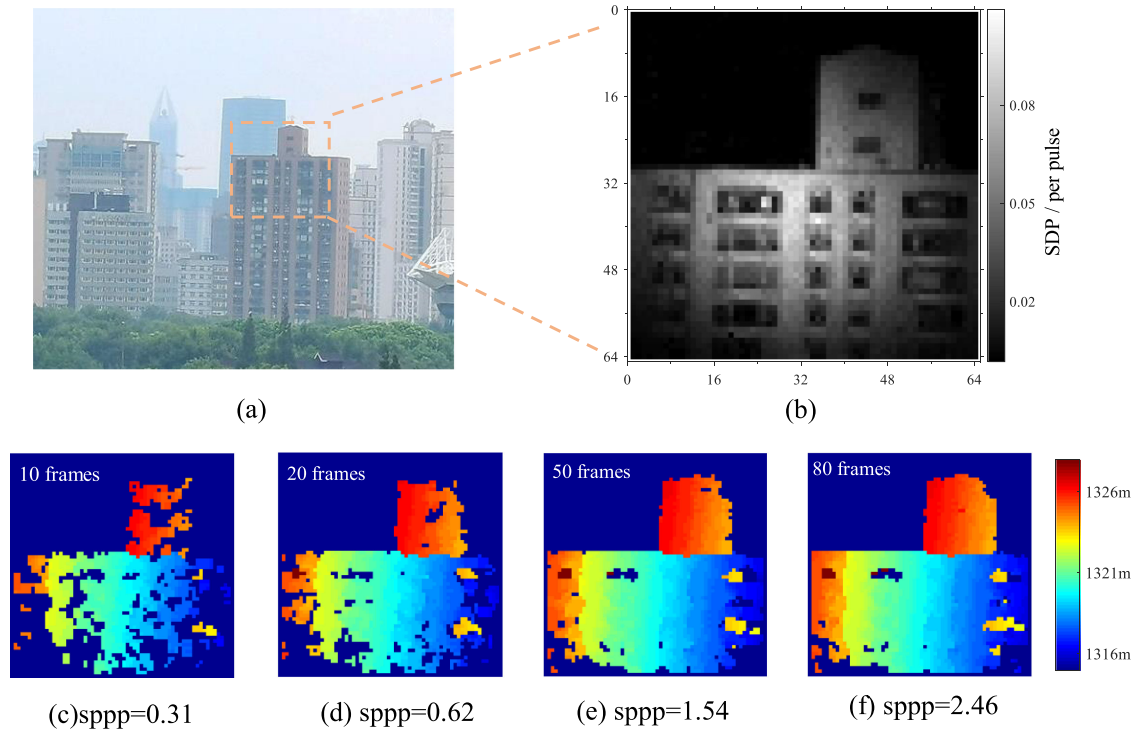


Fig. 5. Depth profiles reconstructed by different extraction strategies, where “sppp” in the figure indicates the signal photon per pulse: (a) Imaging target, (b) Distribution of the signal photon detection probability (SDP), and (c)–(f) Results of the above reconstruction framework under 10, 20, 50, and 80 frame laser pulses, respectively.

TABLE II  
RSNR UNDER DIFFERENT RECONSTRUCTION METHODS

Time	Peak picking	Matched filter	$ST_D$ estimation
1ms	3.90 dB	4.52 dB	11.32 dB
2.5ms	5.92 dB	6.32 dB	15.75 dB

situation where there were a small number of photons, as well as the results extracted by the peak picking and matched filtering methods. Clearly, the spatiotemporal dominant reconstruction strategy described in this study reveals better results than the other two methods. We used the reconstruction signal-to-noise ratio (RSNR) to quantitatively evaluate the imaging performance difference [25], [26], which is expressed as:

$$RSNR = 10 \log_{10} \left( \frac{\|Z_{i,j}^r\|_2}{\|Z_{i,j} - Z_{i,j}^r\|_2} \right) \quad (9)$$

where  $Z_{i,j}^r$  is the reference depth in pixel  $(i, j)$ , and  $Z_{i,j}$  is the estimated depth.  $\|\bullet\|_2$  denotes the L2 norm. Table II presents the RSNR of the three reconstruction methods when the acquisition time is 1 ms and 2.5 ms respectively. The RSNR of the proposed algorithm shows approximately 8.4 dB improvement over the peak picking and matched filtering methods.

Fig. 5 shows the experimental results at larger ranges of approximately 1300 m. Since the echo intensity is inversely proportional to the square of the distance, the average signal photon detection probability per pulse for a single pixel decreases to 3.08%. The decline proportion is consistent with the theoretical

analysis. Fig. 5(b) also shows the probability distribution of each pixel in the detector. For the non-uniformity of the laser energy spatial distribution, buildings near the middle of the field of view scatter more signal photons than edge areas. With such a low signal photon occurrence probability, when the acquisition time is only a few frames, the signal photons per pixel do not even exceed one. However, in Figs. 5(c)–(e), the proposed algorithm still shows good results for when there are few signal photons. The average signal photon per pixel (sppp) is only 0.31, 0.62, 1.54 and 2.46, with frames of 10, 20, 50, 80. The above depth reconstruction framework even works in conditions with average signal photon per pixel less than 1.

Certainly, with the increasing of the frames or number of signal photons, details of the observation target are increasingly revealed. In the above field experiments, it also should be noted that the noise photons have occurrence probabilities up to 78.6% and 64.4%, which are significantly higher than the signal photons. In the second experiment, the occurrence probability of noise photons is 21 times higher than that of signal photons. This also proves that the algorithm has achieved a high performance when estimating depth information of planar-based photon-counting Lidar during daytime.

## V. CONCLUSION

A planar-array-based photon-counting Lidar and its data retrieving method were developed for long-range 3D imaging. The Lidar emits a laser beam with a large divergence angle, and acquires the echo return by an InGaAs/InP  $64 \times 64$  Geiger-mode



avalanche photodiode array to achieve single photon sensitive 3D imaging. Since the laser energy is spread out to 64×64 pixels, the Lidar's single pixel detection probability decreases to <10% at ranges >1 Km. To shorten the data acquisition time for long range observations, a spatiotemporal dominant imaging algorithm based on global optimization theory was proposed. The algorithm even works during daytime while the accumulated number of signal photons <1/pixel. The high efficiency and noise immunity properties of this method make it suitable for photon-limited imaging applications, such as long-range airborne mapping, and moving target imaging.

## REFERENCES

- [1] A. McCarthy, R. J. Collins, N. J. Krichel, V. Fernandez, A. M. Wallace, and G. S. Buller, "Long-range time-of-flight scanning sensor based on high-speed time-correlated single-photon counting," *Appl. Opt.*, vol. 48, no. 32, pp. 6241–6251, 2009.
- [2] D. F. Pierrotet, F. Amzajerjian, B. L. Meadows, R. Estes, and A. M. Noe, "Characterization of 3-D imaging LiDAR for hazard avoidance and autonomous landing on the moon," in *Proc. SPIE Conf. Laser Radar Technol. Appl. XII*, 2007, vol. 6550, pp. 57–65.
- [3] I. Takai, H. Matsubara, M. Soga, M. Ohta, M. Ogawa, and T. Yamashita, "Single-photon avalanche diode with enhanced NIR-sensitivity for automotive LiDAR systems," *Sensors*, vol. 16 no. 4, 2016, Art. no. 459.
- [4] P. F. McManamon, "Review of lidar: A historic, yet emerging, sensor technology with rich phenomenology," *Opt. Eng.*, vol. 51, no. 6, 2012, Art. no. 060901.
- [5] A. McCarthy *et al.*, "Kilometer-range depth imaging at 1550 nm wavelength using an InGaAs/InP single-photon avalanche diode detector," *Opt. Exp.*, vol. 21, no. 19, pp. 22098–22113, 2013.
- [6] Z.-P. Li *et al.*, "Single-photon imaging over 200 km," *Optica*, vol. 8, no. 3, pp. 344–349, 2021.
- [7] J. J. Degnan, "Scanning, multibeam, single photon LiDARs for rapid, large scale, high resolution, topographic and bathymetric mapping," *Remote Sens.*, vol. 8 no. 11, 2016, Art. no. 958.
- [8] A. Mark *et al.*, "Comparison of 32 × 128 and 32 × 32 Geiger-mode APD FPAs for single photon 3D LADAR imaging," in *Proc. SPIE Conf. Adv. Photon Counting Techn. V*, 2011, vol. 8033, pp. 97–108.
- [9] F. Piron, D. Morrison, M. R. Yuce, and J.-M. Redoute, "A review of single-photon avalanche diode time-of-flight imaging sensor arrays," *IEEE Sensors J.*, vol. 21, no. 11, pp. 12654–12666, Jun. 2021.
- [10] M. Henriksson and P. Jonsson, "Photon-counting panoramic three-dimensional imaging using a Geiger-mode avalanche photodiode array," *Opt. Eng.*, vol. 57 no. 9, 2018, Art. no. 093104.
- [11] R. Tobin, A. Halimi, A. McCarthy, P. J. Soan, and G. S. Buller, "Robust real-time 3D imaging of moving scenes through atmospheric obscurant using single-photon LiDAR," *Sci. Rep.*, vol. 11 no. 1, pp. 1–13, 2021.
- [12] G. Chen, C. Wiede, and R. Kokozinski, "Data processing approaches on spad-based D-ToF LiDAR systems: A review," *IEEE Sensors J.*, vol. 21, no. 5, pp. 5656–5667, Mar. 2021.
- [13] J. Tachella *et al.*, "Real-time 3D reconstruction from single-photon LiDAR data using plug-and-play point cloud denoisers," *Nature Commun.*, vol. 10, 2019, Art. no. 4984.
- [14] J. Tachella *et al.*, "Bayesian 3D reconstruction of complex scenes from single-photon LiDAR data," *SIAM J. Imag. Sci.*, vol. 12, no. 1, pp. 521–550, 2019.
- [15] A. Kirmani *et al.*, "First-photon imaging," *Science*, vol. 343, no. 6166, pp. 58–61, 2014.
- [16] S. Dongeek, A. V. K. Kirmani Goyal, and J. H. Shapiro, "Photon-efficient computational 3-D and reflectivity imaging with single-photon detectors," *IEEE Trans. Comput. Imag.*, vol. 1, no. 2, pp. 112–25, Jun. 2015.
- [17] Z.-P. Li *et al.*, "Super-resolution single-photon imaging at 8.2 kilometers," *Opt. Exp.*, vol. 28, no. 3, pp. 4076–4087, 2020.
- [18] Z. Tao *et al.*, "Profiling the pm 2.5 mass concentration vertical distribution in the boundary layer," *Atmospheric Meas. Techn.*, vol. 9, no. 3, pp. 1369–1376, 2016.
- [19] G. Tolt, C. Gronwall, and M. Henriksson, "Peak detection approaches for time-correlated single-photon counting three-dimensional LiDAR systems," *Opt. Eng.*, vol. 57 no. 3, 2018, Art. no. 031306.
- [20] M. Henriksson, H. Larsson, C. Gronwall, and G. Tolt, "Continuously scanning time-correlated single-photon-counting single-pixel 3-D LiDAR," *Opt. Eng.*, vol. 56 no. 3, 2017, Art. no. 031204.
- [21] S. Chen *et al.*, "Learning non-local spatial correlations to restore sparse 3D single-photon data," *IEEE Trans. Image Process.*, vol. 29, pp. 3119–3131, 2020, doi: [10.1109/TIP.2019.2957918](https://doi.org/10.1109/TIP.2019.2957918).
- [22] Y. Kang, L. Li, D. Liu, D. Li, T. Zhang, and W. Zhao, "Fast long-range photon counting depth imaging with sparse single-photon data," *IEEE Photon. J.*, vol. 10 no. 3, Jun. 2018, Art. no. 7500710.
- [23] Z.-P. Li *et al.*, "Single-photon computational 3D imaging at 45 km," *Photon. Res.*, vol. 8, no. 9, pp. 1532–1540, 2020.
- [24] Z. T. Harmany, R. F. Marcia, and R. M. Willett, "This is spiral-tap: Sparse Poisson intensity reconstruction algorithms-theory and practice," *IEEE Trans. Image Process.*, vol. 21, no. 3, pp. 1084–1096, Mar. 2012.
- [25] A. Halimi *et al.*, "Restoration of intensity and depth images constructed using sparse single-photon data," in *Proc. 24th Eur. Signal Process. Conf.*, 2016, pp. 86–90.
- [26] A. M. Pawlikowska, A. Halimi, R. A. Lamb, and G. S. Buller, "Single-photon three-dimensional imaging at up to 10 kilometers range," *Opt. Exp.*, vol. 25, no. 10, pp. 11919–11931, 2017.